

Free Form Lensing Implications for the Collision of Dark Matter and Gas in the Frontier Fields Cluster MACSJ0416.1-2403

Jose M. Diego^{1*}, T. Broadhurst^{2,3}, S. M. Molnar⁴, D. Lam⁵, J. Lim⁵,

¹*IFCA, Instituto de Física de Cantabria (UC-CSIC), Av. de Los Castros s/n, 39005 Santander, Spain*

²*Fisika Teorikoa, Zientzia eta Teknologia Fakultatea, Euskal Herriko Unibertsitatea UPV/EHU*

³*IKERBASQUE, Basque Foundation for Science, Alameda Urquijo, 36-5 48008 Bilbao Spain*

⁴*Department of physics, National Taiwan University, Taipei 10617, Taiwan.*

⁵*Department of Physics, The University of Hong Kong, Pokfulam Road, Hong Kong*

Draft version 29 March 2022

ABSTRACT

We present a free form mass reconstruction of the massive lensing cluster MACSJ0416.1-2403 using the latest Hubble Frontier Fields data. Our model independent method finds that the extended lensing pattern is generated by two elongated, closely projected clusters of similar mass. Our lens model identifies new lensed images with which we improve the accuracy of the dark matter distribution. We find that the bimodal mass distribution is nearly coincident with the bimodal X-ray emission, but with the two dark matter peaks lying closer together than the centroids of the X-ray emission. We show this can be achieved if the collision has occurred close to the plane and such that the cores are deflected around each other. The projected mass profiles of both clusters are well constrained because of the many interior lensed images, leading to surprisingly flat mass profiles of both components in the region 15 – 100kpc. We discuss the extent to which this may be generated by tidal forces in our dynamical model which are large during an encounter of this type as the cores *graze* each other. The relative velocity between the two cores is estimated to be about 1200 km/s and mostly along the line of sight so that our model is consistent with the relative redshift difference between the two cD galaxies ($\delta z \approx 0.04$).

Key words: galaxies:clusters:general; galaxies:clusters:MACSJ0416.1-2403; methods:data analysis; dark matter

1 INTRODUCTION

Strong gravitational lensing is entering a new era of enhanced precision with the arrival of the new Hubble data from the CLASH Postman et al. (2012a) and now from the Frontier Fields¹ (HFF, hereafter) programs. Clusters observed under these programs routinely contain tens of multiply lensed systems with well defined colours to help identify counter-images. The cluster RXJ1532.8+3021 is a notable exception where CLASH data does not reveal any strongly lensed system. Weak lensing analysis suggests a very low concentration for this cluster Merten et al. (2014). In X-rays, the cluster shows two prominent cavities in opposite directions, a clear signature of a very powerful black hole in

the central galaxy supported by VLA radio observations of the associated jets. The picture in this cluster is consistent with the existence of a supermassive blackhole with a mass $M_{BH} \sim 10^{10} M_{\odot}$ Hlavacek-Larrondo et al. (2013).

The abundance of strong lensing observables allows for an unprecedentedly detailed reconstruction of the dark matter distribution that is responsible for the lensing distortions. The lensing models have evolved to take increasing advantage of the improvement in data quality. The most massive clusters, with the largest quantity of strong lensing information, are often the most complex, undergoing dynamical evolution. Parametric models are most powerful for relaxed systems but arbitrary choices have to be made when representing substructures with idealized halo components Kneib et al. (1996); Sharon et al. (2005); Halkola, Seitz & Panella (2006); Limousin et al. (2007); Nakajima & Morikawa (2007); Nieuwenhuizen & Morandi (2013)

¹ <http://www.stsci.edu/hst/campaigns/frontier-fields/>

We have tackled this problem in two ways previously, with application to A1689. Firstly, by a compromise *semi-parametric* method which assumed mass approximately traces light Broadhurst & et al. (2005a) has been successful in dealing with this problem, and useful for locating many sets of multiple images and has been developed further for the clash data Zitrin et al. (2011, 2012, 2013) but is still does not allow for the possibility that the dynamics of the dark may differ from that of the member galaxies. A fully general free-form approach was developed by Diego et al. (2005a,b, 2007), based on a pixellated grid representing the lens plane. This does not provide sufficient accuracy to find new systems so that it must rely on lensed systems found by other models. More recently we have found it very advantageous to incorporate the known position of member galaxies in the grid solution, so that meaningful solutions can be found Sendra et al. (2014); Diego et al. (2014), and here we employ this method to model the complex merging cluster MACSJ0416.1-2403 (MACSJ0416 hereafter), relying on our own image identifications. free form approach of dividing

The success of the above approaches has relied also on a better understanding of the optimization of colour information. By utilising overlapping broad bands of the CLASH program covering the UV to the NIR, we can maximize the photometric redshift accuracy possible with Hubble and have provided reliable examples of the most distant galaxies known, as in the case of the $z \simeq 11$ candidate lensed by MACS0647 (Coe et al. 2013), where multiple images are identified both photometrically and geometrically. Improving on the CLASH program, the current FF program is destined to leave a legacy of exquisite quality data on gravitational lenses. The superior depth attained by the FF program, promises a wealth of faint multiply lensed galaxies, as the first examples are already showing (Zheng et al. (2014); Atek et al. (2014); Johnson et al. (2014); Richard et al. (2014); Jauzac et al. (2014), Lam et al. 2014 in preparation).

The cluster A2744 was the first one being released within the HFF program. More recently, new data from the FF was made available on the cluster MACSJ0416.1-2403, a massive merging galaxy cluster at redshift $z = 0.4$. A first analysis based on CLASH data on MACSJ0416 was performed by Zitrin et al. (2013) (Z13 hereafter). In that paper the authors identified 70 multiple images from 23 background galaxies. The strong lensing analysis of Z13 reveals a very elongated structure for the dark matter distribution. The addition of the new data from the FF program helps in clarifying some of the systems published in Z13. In a very recent paper, Jauzac et al. (2014) (J14 hereafter), published a parametric solution and extends the original set of system candidates of Z13 to more than 50 systems. Also in two additional very recent papers, six of the FF clusters are studied using strong lensing Johnson et al. (2014), or a joint strong-weak lensing analysis Richard et al. (2014). Among these clusters, the cluster MACSJ0416 is also included. A detailed comparison of our results with those derived using parametric methods is beyond the scope of this paper and will be considered in a future paper.

Colliding clusters are of special interest for understanding the properties of DM particles and the dynamics of the infalling systems through hydrodynamical modelling such as that of the bullet cluster Springel & Farrar (2007); Mastropi-

etro & Burkert (2008) and more recently for the bullet like 'El Gordo' system, Molnar & Broadhurst (2014). In particular, colliding clusters have been used to set stringent limits on the scattering cross section (see Kahlhoefer et al. (2014) for a recent discussion). In Kahlhoefer et al. (2014) the authors conclude that small separations between the DM and the luminous matter (galaxies) are only possible right after the collision but not on more relaxed systems. If MACSJ0416 is in the turnaround phase (as suggested in citeMann2012) we should not expect a separation between the DM and the luminous matter (galaxies) for values of the dark matter cross section $\sigma/m \sim 1 \text{cm}^2/g$ or less. In de Laix, Scherrer & Schaefer (1995); Spergel & Steinhardt (2000) they discuss how self-interacting dark matter can explain the flattening of cluster cores. In addition, Rocha et al. (2013) study simulations of self-interacting DM and derive some interesting conclusions that will be discussed later.

It is possible to derive constraints on the DM self-interaction cross-section from the fact that such systems have survived the collision. If self-interaction occurs between DM particles, one would expect a shift between the positions of the DM peak and galaxy positions Markevitch et al. (2004). A detailed study of the mass distribution responsible of the lensing distortions around the central galaxies in MACSJ0416 has the potential to reveal such shifts. The pronounced elongation of MACSJ0416 might help in distinguishing this possible shift.

In a recent paper based on X-ray and optical data, Mann & Ebeling (2012) classifies the cluster MACSJ0416 as a clear example of a post-collision merger and they add that the cluster could be even in the phase after turnaround. However, due to relatively poor X-ray data, the pre-collision scenario can not be ruled. Deeper observations in X-rays could confirm the premerger scenario if an enhancement in the temperature is observed between the two subclusters, Ricker & Sarazin (2001). Chandra data reveals an offset between the peaks in the X-ray emissivity and the cD galaxies, Mann & Ebeling (2012), which is consistent with the post-merger scenario (see also figure 1). The fact that one of the X-ray peaks is ahead of one the main cD galaxies would be consistent with the turnaround scenario.

Through the paper we assume a cosmological model with $\Omega_M = 0.3$, $\Lambda = 0.7$, $h = h_{100} = 100 \text{km/s/Mpc}$. For this model, 1 arcsec equals $3.87 \text{kpc}/h_{100}$ at the distance of the cluster.

2 FF DATA

In this paper we used public imaging data obtained from the ACS (filters: F450W, F606W and F814W) and the WFC3 (F105W, F125W, F140W and F160W), retrieved from the Mikulski Archive for Space Telescope (MAST). Some of these bands were not available at the time when the analysis of Z13 was made. The new color bands are useful to identify systems that match (or do not match) in color but also to go deeper in magnitude. New observations on this cluster are planned for the near future in the optical bands. The data used in this paper consists of 50% of the data that will be available in the near future.

We combined all the filters into three color bands to produce the color image of the new candidate systems shown in

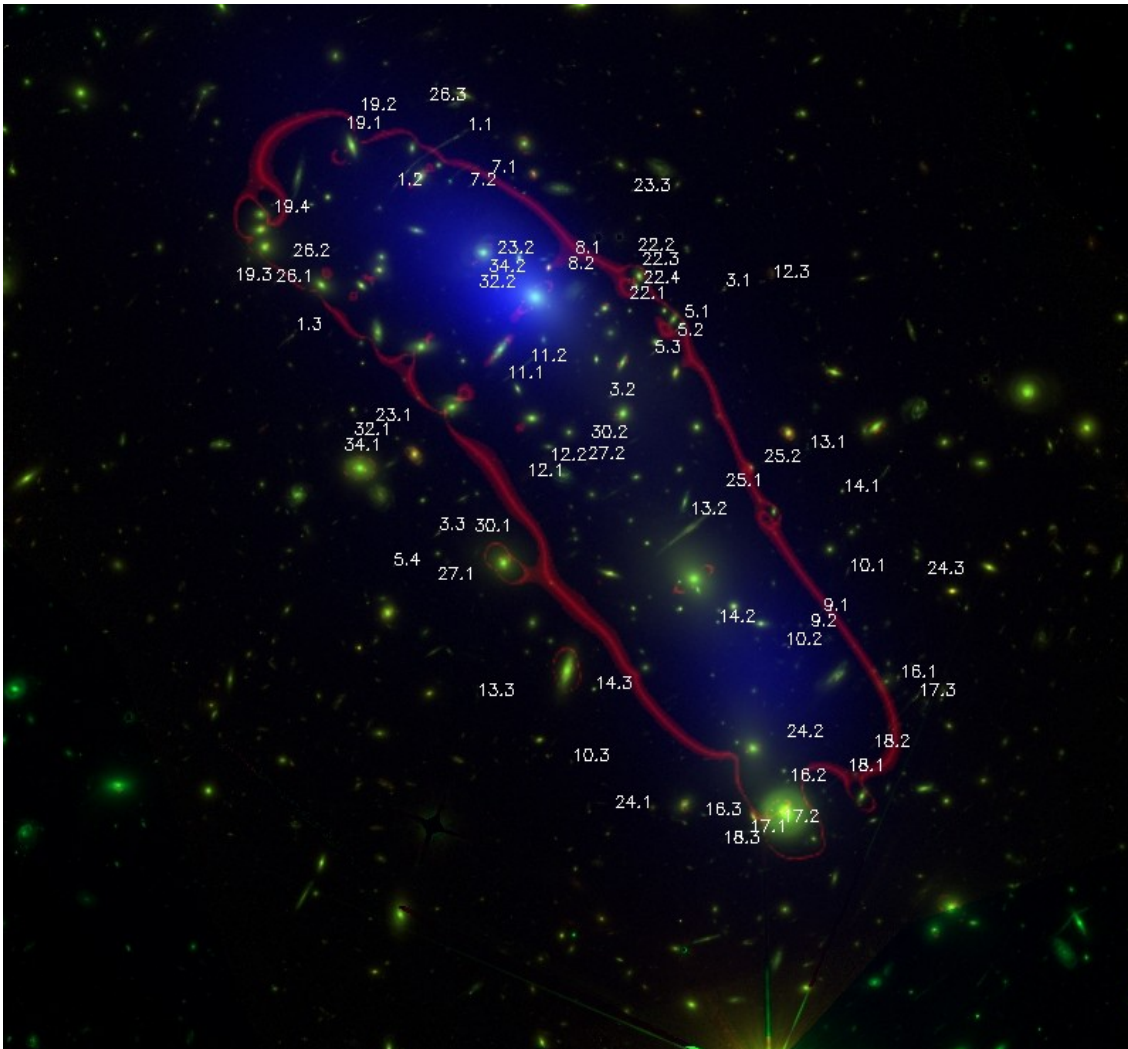


Figure 1. Relative position of the systems used in the reconstruction (part I). The critical curve corresponds to the case i) described in 4.1. The two blue clouds correspond to the peaks of the X-ray emission from Chandra. The field of view is 2.4 arcminutes.

the Appendix. The image was processed in Fourier space to reduce the contribution of large angular scale modes due to diffuse light from the member galaxies and later combined to produce a color image. The Fourier filtering introduces artificial changes in the brightness of sources around bright sources (galaxies and stars). The different angular resolutions of the optical and IR bands introduces also an element of uncertainty when processing the images in Fourier space so images that fall near bright sources may have their colors slightly distorted. We have checked that the colors of our candidates agree in the original color image (that does not include the filtering in Fourier space).

3 LENSING DATA

Our strong lensing data set is primary based on the system identification of Z13. Some of the photometric redshifts in that work have been updated with the recently published ones in J14 (that appeared at the time when we were finalizing this paper). Although the compilation of J14 supersedes the systems published in Z13, we rely on the early

identification of Z13 and leave for a different paper the analysis based on the systems of J14 (some of which are more reliable than others). In that work, the authors extend the original set of 23 systems in Z13 to over 50 candidate systems. A proper comparison of our results and theirs will be published in a separate paper and once the full FF data set is available. However, in section 6 we make a small comparison in one of the new systems that is common to both data sets. Despite the fact that the system used in our work and theirs is different, a simple consistency test shows a high degree of agreement between our solution and theirs.

Our strong lensing data set is listed in table A1 in the appendix. Systems 1 through 23 are taken directly from Z13 and systems 24 through 38 are new candidates identified in this work. Systems 6 and 20 in Z13 are dubious and have been removed after color comparison with the new addition of the IR data from the FF program. Some of the counterimages in Z13 have deliberately not being used in this work as the proximity of multiple candidates makes it difficult to secure the identification. However we should note that most of these counterimages are in general in good agreement with



Figure 2. Relative position of the systems used in the reconstruction (part II). In this case, the critical curves ($z_s = 3$) are for for the cases ii) (red) and iii) (blue) in section 4.1.

our lens model so their inclusion in our analysis should have a small impact in the reconstructed mass. A few of the arclets in Z13 have been rematched, in particular 12.3 (we use a different candidate from Z13 at one of their predicted positions) 15.3, 19.4 and 22.4. The new selection of systems is based on a combination of color matching (after including the new data from the FF program) and comparison with a lens model. The lens model used for this comparison is obtained after using the 23 original systems of Z13 and our free-form algorithm. The lens model allows us also to identify new system candidates in the new optical+IR data by predicting the positions where counterimages are expected (for a given redshift) and also by predicting the right orientation and morphology of the lensed images. A few examples showing relensed images and involving systems 1,2,3 and 4 are shown in the appendix in figure A7. The relensed image of the special new system 35 is shown (and discussed) also in section 6.

shown in the appendix². The relative positions of the images defining our lensing data set is shown in figures 1 and 2. The data set has been divided into two groups for clarity purposes. Figure 1 shows part of the data set together with one of the critical curves derived in this work (see section 4.1). In blue color, we also show an adaptively smoothed version of the X-ray emission from Chandra data³ for reference. The Chandra data has been smoothed using the code ASMOOTH, Ebeling, White & Rangarajan (2006). Figure 2 shows the remaining systems together with two critical curves corresponding to two alternative solutions (see section 4.1)

Stamps from the complete data set in table A1 are also

² also available in this website
http://www.ifca.unican.es/users/jdiego/MACS0416_March2014/Systems/
³ ivo://ADS/Sa.CXO#obs/10446

4 RECONSTRUCTION METHOD

We use the improved method, WSLAP+, to perform the mass reconstruction. The reader can find the details of the method in our previous papers (Diego et al. 2005a,b, 2007; Ponente & Diego 2011; Sendra et al. 2014; Diego et al. 2014). Here we give a brief summary of the most essential elements.

Given the standard lens equation,

$$\beta = \theta - \alpha(\theta, \Sigma(\theta)), \quad (1)$$

where θ is the observed position of the source, α is the deflection angle, $\Sigma(\theta)$ is the surface mass density of the cluster at the position θ , and β is the position of the background source. Both the strong lensing and weak lensing observables can be expressed in terms of derivatives of the lensing potential.

$$\psi(\theta) = \frac{4GD_l D_{ls}}{c^2 D_s} \int d^2\theta' \Sigma(\theta') \ln(|\theta - \theta'|), \quad (2)$$

where D_l , D_{ls} and D_s are the angular diameter distances to the lens, from the lens to the source and to the source, respectively. The unknowns of the lensing problem are in general the surface mass density and the positions of the background sources. As shown in Diego et al. (2007), the strong lensing problem can be expressed as a system of linear equations that can be represented in a compact form,

$$\Theta = \Gamma X, \quad (3)$$

where the measured strong lensing observables are contained in the array Θ of dimension $N_\Theta = 2N_{SL}$, the unknown surface mass density and source positions are in the array X of dimension $N_X = N_c + N_g + 2N_s$ and the matrix Γ is known (for a given grid configuration and fiducial galaxy deflection field) and has dimension $N_\Theta \times N_X$. N_{SL} is the number of strong lensing observables (each one contributing with two constraints, x , and y), N_c is the number of grid points (or cells) that we use to divide the field of view. In this paper we consider a regular grid of $N_c = 32 \times 32 = 1024$ cells covering the field of view shown in figures 2 and 2 (2.4 arcminutes). N_g is the number of deflection fields (from cluster members) that we consider. In this work we test three different configurations for the deflection field where N_g is equal to 1 (all member galaxies conform a unique deflection field) or $N_g = 3$ which corresponds to the case where the two main cD galaxies are considered independently from the rest of the cluster members. See section 4.1 for details of the three configurations. N_s is the number of background sources (each contributes with two unknowns, β_x , and β_y , see Sendra et al. (2014) for details). The solution is found after minimizing a quadratic function that estimates the solution of the system of equations 3. For this minimization we use a quadratic algorithm which is optimized for solutions with the constraint that the solution, X , must be positive. Imposing the constrain $X > 0$ also helps in regularizing the solution as it avoids large negative and positive contiguous fluctuations.

4.1 Fiducial galaxies

The member galaxies defining the fiducial field are all elliptical galaxies selected from the red sequence plus two

very luminous (and possibly massive) spiral galaxies that lay near the critical curves. The selected galaxies are shown in figure 4. In the reconstruction, we need to assume some masses for the fiducial field (cluster members). We explore three different alternatives.

i) The light of the galaxies traces their mass (LTM). We select the member galaxies from the red sequence and make their masses proportional to the optical flux in the F814w band. The total mass of the galaxy field is then normalized to have $7.0 \times 10^{13} M_\odot/h$. In this case there is only one parameter, C_1 , in the vector X that re-scales the entire fiducial field.

ii) Like the above but the two main cD galaxies have now their own parameter C , hence we have three parameters C_1 for the non-cD galaxies, C_2 for the NE cD galaxy and C_3 for the SW galaxy.

iii) Instead of assuming that the mass follows the light, we associate a circularly symmetric NFW profile to each galaxy, Navarro, Frenk & White (1997). The masses take different values than the ones in cases i) and ii) and also we use 3 fiducial fields like in case ii).

The fiducial masses for these three cases are shown more explicitly in figure 4 below.

5 DARK MATTER DISTRIBUTION

The mass reconstruction is shown in figure 3 for the three cases discussed in section 4.1. The field of view has been rotated by 45 degrees (counterclockwise) so the NE cluster is now at the left and the SW cluster is now to the right. Projections along the main axes in the cluster are shown in the left and bottom panels for each case.

A striking result is the relatively high symmetry between both subclusters suggesting a mass ratio of 1:1 for this merger. From the morphological point of view, both subclusters seem to have similar masses and morphologies when projected in the two orthogonal directions. The extended soft dark matter halo is divided in two sub-halos, each associated with one of the two cD galaxies in the cluster. These sub-haloes do not show a peculiar symmetry, in particular there is no clear evidence for the elliptical spheroids assumed in parametric methods but rather the soft dark matter halo shows a rather irregular shape. When comparing the 3 reconstructions, we find that the assumptions made on the fiducial field play a secondary but not entirely negligible role. Comparing cases i) and ii), the solution seems to prefer the two main cD galaxies having larger mass associated to their halos. The same result is observed when all the haloes are assumed to follow a (symmetric) NFW profile as seen in case iii). It can be also observed, that when the galaxies take more mass this is at the expense of the mass in the grid component, maintaining the total mass more or less constant. This type of degeneracy is expected in this particular cluster due to the relatively small number of radial arcs that fall close to the main cD galaxies. The mass distribution around these galaxies remains then relatively unconstrained.

Figure 4 shows the contours of the soft component (grid only) superimposed on the fiducial galaxies for the 3 cases described in subsection 4.1. The three cases reproduce almost identical results around the position of the critical curves. However, small differences can be appreciated in the

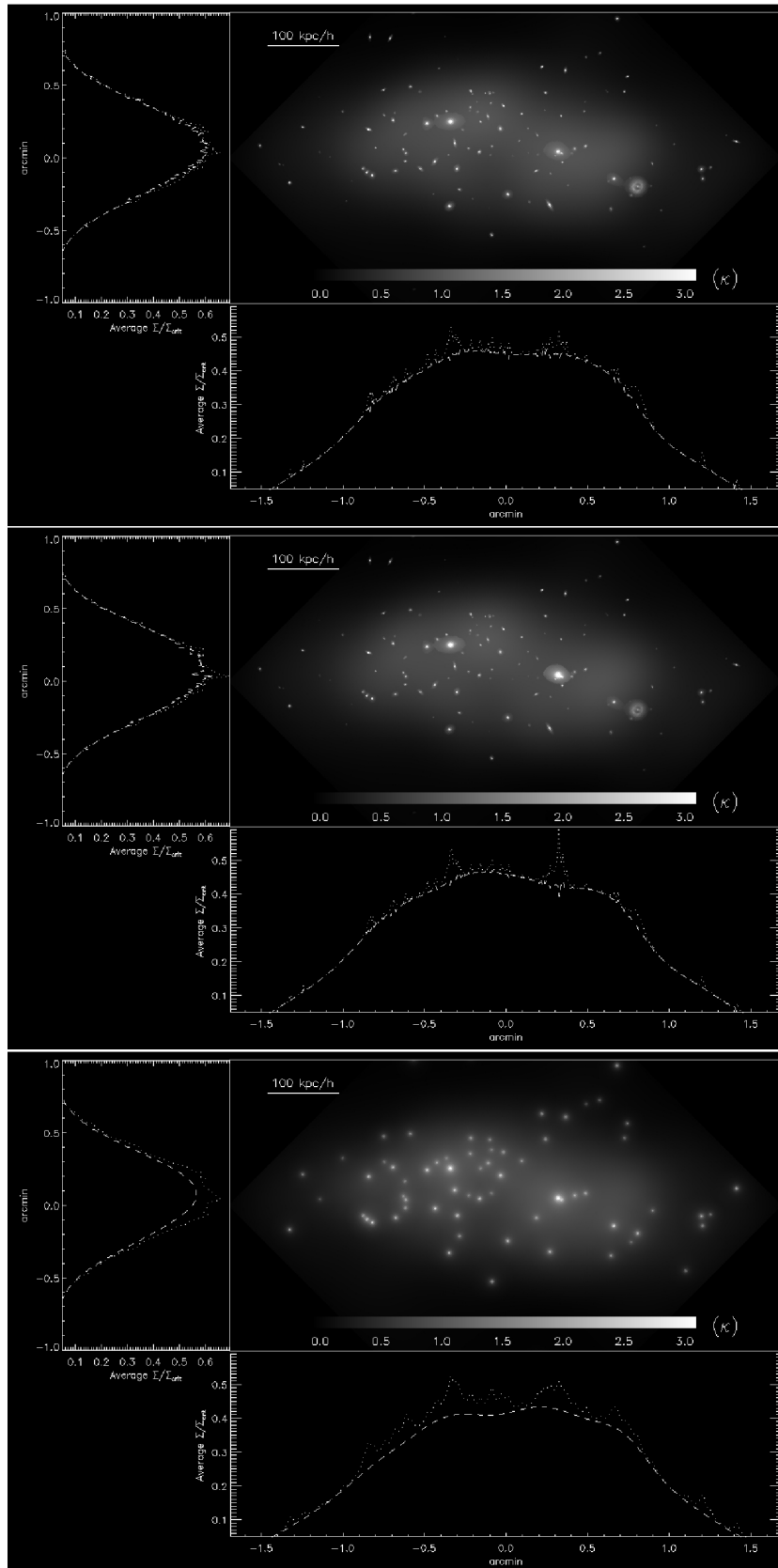


Figure 3. Reconstructed mass in MACSJ0416 in units of its convergence (for $z_s = 3$). 2-dimensional convergence (κ) map and the mean value of the projected convergence along the y and x axis respectively. The two curves correspond to the total mass (dotted) and to the grid-only mass (dashed). The convergence maps have been saturated beyond $\kappa=3$ for clarity purposes. The top plot is for case i) described in section 4.1. The middle plot is for case ii). The bottom plot is for case iii).

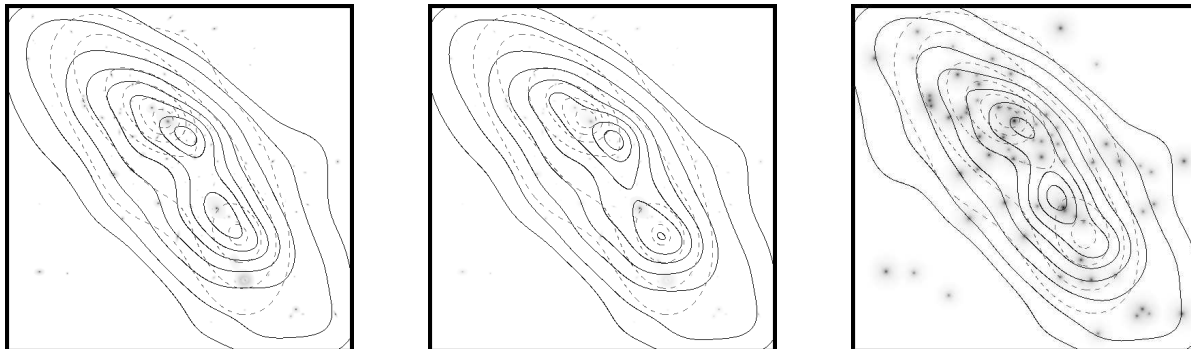


Figure 4. Contours of the reconstructed mass of the grid component compared with the fiducial galaxy field. From left to right, cases i), ii) and iii) respectively and described in section 4.1. In all cases, the contours correspond to 0.1,0.2,0.4,0.6,0.75,0.85,0.93, and 0.98 times the maximum of the soft component. In all panels, the dashed contours shows the smoothed X-ray emission from Chandra.

central region with the models showing some dependency with the assumptions made about the central cD. Interestingly, a shift can be appreciated between the position of the cD galaxies and the peak of the diffuse component when we assume that the mass in the galaxies traces their light, case i). The shift is more pronounced when the two cD galaxies are unlocked from the remaining galaxies, case ii). When the two cD galaxies are locked to the other galaxies, case i), the grid takes on the possible missing mass around these two galaxies shifting the peak of the diffuse mass closer to the position of the galaxies. This is made more evident in figure 3 above, where in case ii) we appreciate a higher contribution from the main cD to the cluster mass than in case i). In case iii) we do not observe a significant shift between the peaks of the soft dark matter halos and the 2 main galaxies. However, in this case, the more extended nature of the fiducial galaxies reduce the relative importance of the grid as the superposition of the extended haloes in the fiducial galaxies can reproduce some of the soft features that otherwise would be reproduced by the grid. Case iii) can be considered as a case where the galaxies compete more with the grid than in cases i) or ii) or more mathematically, the base defined by the grid+galaxies is less orthogonal than the other two cases. When comparing the soft DM component with the X-ray emission, there are small offsets between the two components but these offsets depend on the assumptions made for the fiducial galaxies. Also, the peak in the X-ray emission is now well defined and depends on the resolution at which the X-rays are smoothed. Deeper X-ray observations are needed to better constrain the position of the X-ray peaks.

The fact that the DM peak from the soft dark matter halo (grid) may be shifted with respect to the position of the cD galaxies is an interesting feature. Since the galaxies can be truly considered as collisionless, the DM could have its peak shifted with respect to the main galaxies if they have a significant cross section, σ/m . This case has been recently studied by Kahlhoefer et al. (2014) where they consider a

value of $\sigma/m \approx 1 \text{ cm}^2/\text{g}$. They find that small shifts are expected only immediately after the collision between the two clusters. The peaks of the DM and the dominant galaxy quickly converge to the same point shortly after the collision. However, they also find that the baryonic and the DM particles exhibit different profiles with the galaxies showing a tail moving ahead (in the direction of the movement of the halo) of the DM halo and the DM showing a more elongated tail in the opposite direction of the movement.

The contours in figure 4 show a clear elongation of the DM haloes in the axis of the merger. Interestingly, the halo in the SW shows a more pronounced elongation. This picture is consistent with the situation discussed in Kahlhoefer et al. (2014) if a non-negligible value for $\sigma/m \approx 1.5h^{-1} \text{ cm}^2/\text{g}$ is assumed.

Another possibility is that the elongation may be due to our reconstructed mass distribution being also sensitive to the projected mass of the plasma. If the plasma is displaced with respect to the DM, this could produce an elongation in the projected mass distribution in the direction of the displacement. This possibility will be discussed in more detail in section 7. The fact that the elongation traces the shape of the maxima of the X-ray contours suggests that this scenario is possible. In Lan et al. (2014), a similar excess of mass not directly linked to the observed galaxies is also found in a region with significant X-ray emission.

Regarding the masses contained in the galactic component, for case i), the derived total mass of the fiducial galaxies is $8.21 \times 10^{12} M_{\odot}/h$. For case ii), the derived masses of the two main cD galaxies are $1.13 \times 10^{12} M_{\odot}/h$ for the NE cD galaxy and $1.95 \times 10^{12} M_{\odot}/h$ for the SW cD galaxy. The combined total mass of the remaining fiducial galaxies equals $5.36 \times 10^{12} M_{\odot}/h$. For case iii), the derived masses of the two main cD galaxies are $1.41 \times 10^{12} M_{\odot}/h$ for the NE cD galaxy and $1.34 \times 10^{12} M_{\odot}/h$ for the SW cD galaxy. The combined total mass of the remaining fiducial galaxies equals $2.08 \times 10^{13} M_{\odot}/h$. The higher galaxy masses in case

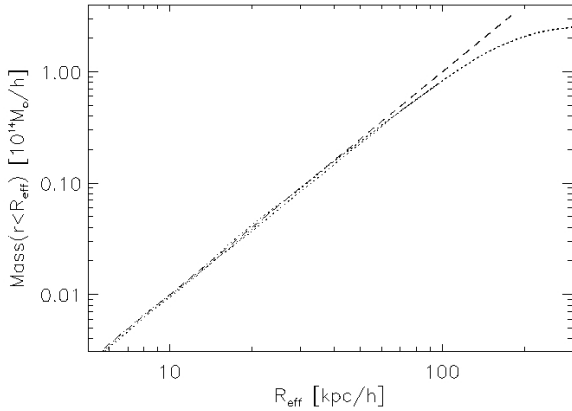


Figure 5. The dotted line corresponds to the integrated mass as a function of effective radius (see text). The dashed line is a power law, $M \propto R_{eff}^2$

iii) can be attributed to their larger angular size that takes away some of the mass from the grid component.

In order to get an estimate of the integrated mass as a function of radius, and given the high asymmetry of this cluster, we integrate the masses following the contours of the cluster. Using the contours (similar to the ones shown in figure 4) we can define an effective radius, $R_{eff} = \sqrt{A/\pi}$, where A is the area enclosed by a given contour. By setting different thresholds in the projected mass maps we can build a set of contours, each with a given enclosed area, A , and R_{eff} . The integrated mass is shown in figure 5 as a function of R_{eff} . The mass in the y-axis corresponds to the combined total mass of the two sub-clusters above a given threshold (with an associated radius, R_{eff}). In figure 5 we also show a power law, $M(< R_{eff}) = 10^{-4} (R_{eff}/h^{-1} \text{kpc})^2 M_{\odot}/h$ that fits nicely the integrated mass in the regime 5 – 50 kpc/h. A mass growing as the square of the radius is expected for a surface mass density that is constant with radius. The nearly-flat behaviour of the surface mass density in the region 5 – 50 kpc/h is made more evident when we compute the radial profiles of each subcluster after masking the other one out.

Figure 6 shows the circularly-averaged profiles for each subcluster in the 3 cases discussed above. The centre of the cluster is the corresponding cD galaxy. The dotted line is for the NE cluster and the dashed line is for the SW cluster. The profiles for each subcluster are computed after excluding the other one from the calculation. The division between the two clusters (and the mask) is defined by a straight line going between the bottom left corner to the top-right corner of figure 4. The profile is computed in units of the critical surface mass density assuming a redshift of $z_s = 3$. The two profiles are almost identical, both in their amplitudes as well as in their slopes with the exception of the very central region where the cD profile dominates. The profiles beyond 30 arcsec (115 kpc/h) show a sharp decline. Part of this decline is due to the fact that the profile is an average of an elongated surface mass density distribution. Beyond 30 arcseconds, the profiles behave very differently in the two orthogonal directions as shown in figure 3. Hence, we should expect the profile to retain some of the features in the the

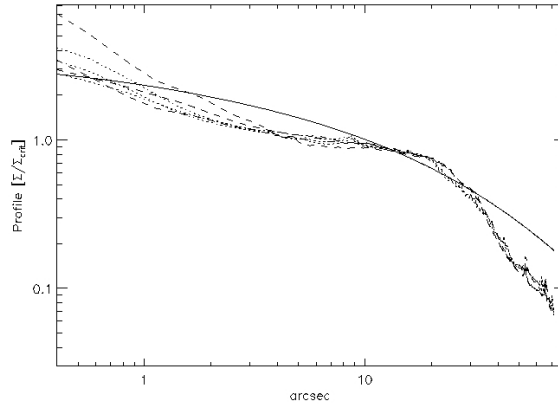


Figure 6. Profiles of the two cluster haloes for the three different cases. The profiles are centered in the two main cD galaxies. The NE halo corresponds to the dotted lines and the SW halo corresponds to the dashed lines. In the computation of the profiles, we have masked the other half of the cluster. The solid line corresponds to a projected NFW model with a truncation radius of $R_{200} = 2.5 \text{ Mpc}/h$ and $C = 10$.

x and y projected profiles in figure 3. However, is important to emphasize that the profiles in figure 6 are derived for each subcluster while masking the other one so the highly asymmetric distribution of the double cluster is somewhat attenuated. Another reason for the decline of the profile at large radii is the lack of constraints. As shown in our earlier works, our algorithm underestimates the real dark matter distribution when going into the outer radii where there is no more strong lensing constraints. On the other extreme, the inner part of the profiles depend on the assumptions made in the profiles of the fiducial field for the member galaxies and it is affected by uncertainties on these profiles. The lack of constraints in the very central region limits also the accuracy at which this part of the profile can be estimated. However, the mass distribution in the range 5-30 arcseconds (20 – 115 kpc/h) can be trusted. The mass profiles in this range show little dependency with the assumptions made on the fiducial field. In figure 6 we also plot as a reference the projected surface mass density (in terms of the same critical surface mass density) of a NFW profile. A simple NFW profile can not fit the mass distribution of each subhalo. Modifications of the NFW profile, like a cored NFW profile would produce a better fit.

6 THE CURIOUS CASE OF SYSTEM 35

In this section we explore in more detail the new system 35. Despite being a relatively bright system with distinctive features, it was not matched in the previous work of Z13. The reason maybe the fact that there are two possible images that could be the predicted third counterimage of this system. Usually, these kind of ambiguity is found in systems that exhibit none or few morphological features, are unresolved or too faint. However, system 35 shows a relatively complex morphological and color-rich structure that should, in principle, make it relatively easy to identify its counterimage(s). This new system is also interesting because the two central counterimages are very close to the northern cD galaxy and

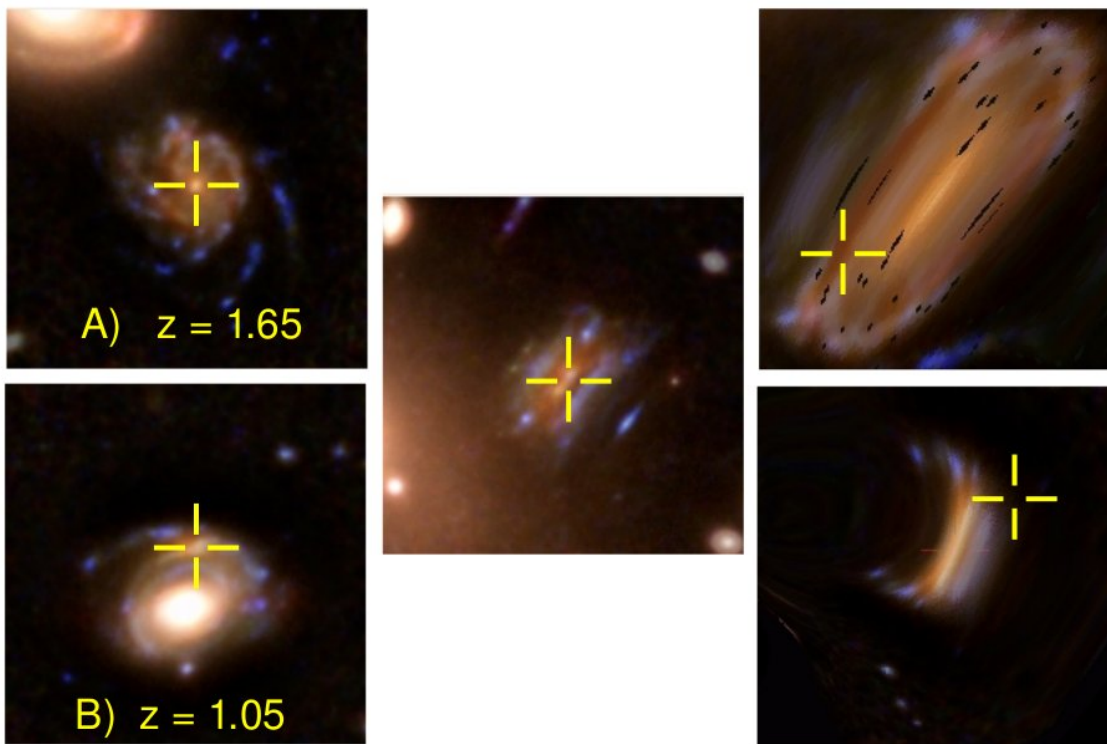


Figure 7. The two possible configurations for system 35. The two counterimages 35.2 and 35.3 are shown in the middle column. The left column shows the two possibilities, A and B for the counterimage 35.1, each one at a different redshift. The right column shows the predicted re-lensed image based on our model for case ii) and using the corresponding delensed image on the left column. The situation is similar for the models of case i) and iii). The field of view is 7.2 arcseconds in all cases. The crosses mark the observed positions.

they are sensitive to the density profile in the innermost part of the cluster. Images 35.2 and 35.3 are challenging to reproduce by lens models due to the fact that they are merging into a single image (or splitting from one single image) and hence are very sensitive to the small fluctuations in the gravitational potential at the centre but at the same time this offers a good opportunity to study in detail the potential surrounding the northern cD galaxy. In figure 7 we show the two possibilities for system 35, option A at redshift $z_s \approx 1.65$ and option B at redshift $z_s \approx 1.05$ (these redshifts are estimated from the lens model). The same plot shows also the predicted lensed images based on the two possibilities for the third counterimage. Both options reproduce the position, orientation and some of the color and morphological features of the observed images. The apparent size of the released image is better reproduced in the option B. On the other hand, option A contains a very compact nucleus that is more consistent with the observed double nucleus in 35.2 and 35.3 while the nucleus appears more difuminated in option B. Based on the presence of the nucleus we adopt option A as the counterimage but noting that option B is equally valid (in terms of being fit by the model). Preliminary results (work in preparation) shows that the size is better reproduced with option A when we consider a multiresolution grid that increases the resolution of the matter distribution around the central NW cD galaxy (see figure 8).

Interestingly, in the recent paper by J14, the authors consider option B in their analysis although they assume a slightly different redshift for the system ($z_s = 1$). Although

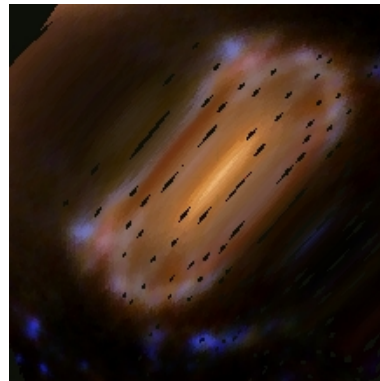


Figure 8. As in figure 7, predicted system 35 for option A in the case of a multiresolution grid. The scale and position is the same as in the case of option A in figure 7.

a more detailed and quantitative comparison with J14 will be done in a subsequent paper, the fact that their alternative definition of system 35 (redefined as system 28 in their work) is coincident with the option B for system 35 discussed above, suggests that, at least in the regions of the cluster probed by system 35, the free-form model derived in this paper and the parametric model derived in J14 are consistent to a high degree. The ambiguity in system 35 can be eliminated once a spectroscopic redshift of the system 35 is obtained. The redshift will unambiguously determine which one of the options, A or B, is the correct one. This system

is a good text book example of the ambiguity inherent to strong lensing where highly distorted images are difficult to match even if these images are bright and well resolved.

7 GEOMETRY AND DYNAMICS OF THE MERGER

Multiwavelength observations offers the opportunity to interpret the observations in the context of the dynamical state and geometry of the cluster. The fact that an offset is observed between the X-ray peaks and the inferred local minima of the gravitational potential (at the position of the cD galaxies) suggests that the plasma is being affected by dynamical friction and is leaving the potential well. These scenarios have been observed in different clusters with the most famous being the *bullet* cluster. In these cases, the plasma always lays behind the moving gravitational potential. In the bullet cluster, the cluster is observed after the collision has happened and the two clusters are moving in a plane that is close to the plane of the sky so projection effects are small. In our case, there is no obvious way to tell what the plane of the collision is by looking at the DM and lensing maps. If we assume that the collision is taking place in the plane of the sky, the SW clump shows the peak of the X-rays displaced with respect o the DM peak but in the opposite side that one would expect if a collision has already happened. If the collision has not happened yet, and the two clusters are on course for their first core passage, the X-ray peak in the SW would be on the right side but the magnitude of the shift is too large since the plasma is expected to dissociate from the DM at the time of closest approach.

Alternatively, if the collision happens in a plane that is normal to the plane of the sky, projection effects can help to explain the relative positions of the DM and X-ray peaks. Figure 9 shows an example from a hydrodynamical simulation that resembles the case of MACSJ0416. Like in figure 4, solid contours correspond to the DM component and dashed contours to the X-ray surface brightness. Our simulation is projected along an axis with 21 degrees inclination angle relative to the line of sight. The morphology is similar: the peaks of the dark matter and X-ray emission are almost in the same line. The dark matter peaks are located closer to each other. The large offset between the peak of the dark matter and X-ray emission of the infalling cluster is due to the ram pressure separating the gas form the dark matter component as it passes through the main cluster. With virial concentration parameters of 5 and 8, our simulation has smaller masses (2 and $0.5 \times M_{\odot}$) and a larger infall velocity (4500 km/sec) and produce a larger offset between the dark matter and the X-ray emission, therefore it is likely that a smaller infall velocity is necessary to produce the observed morphology. The offsets between the peaks of the dark matter surface density and X-ray emission in the merging cluster are important in terms of understanding the physics of the collision (i.e., initial masses of the two components, the impact parameter and infall velocity).

In this simulation, the clusters are moving in a direction that is close to the line of sight and due to the projection effects the X-ray peak in the SW seems to be located ahead of the DM peak in the SW. However, the 3D simulation shows that the X-ray peak is already behind the DM peak as ex-

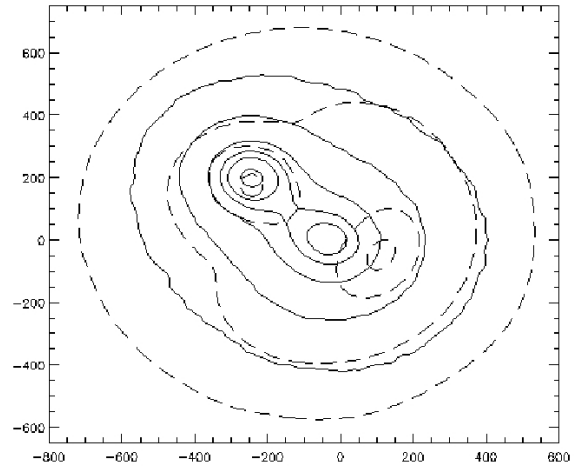


Figure 9. Simulated cluster with the two clumps moving along the line of sight and the X-rays (dashed contours) showing an offset with respect to the DM (solid contours) to the right of the south clump due to projection effects. The axis are in kpc.

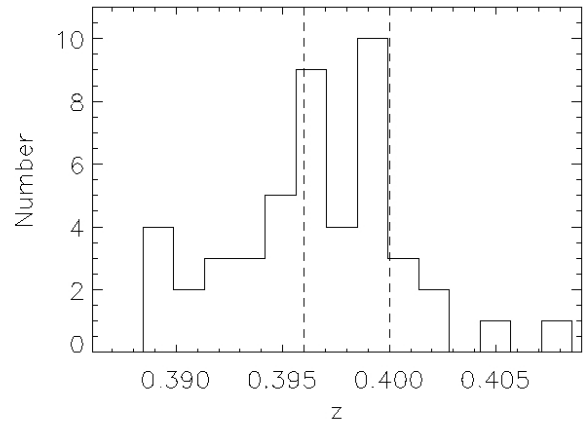


Figure 10. Histogram of the galaxies with spectroscopic redshifts in the field (see Ebeling et al. 2014)

pected. The scenario where the collision happens in an axis close to the line of sight is also supported by the difference in spectroscopic redshift between the two cD galaxies. These redshifts were recently published in Ebeling, Ma & Barrett (2014). The NE cD galaxy has an spectroscopic redshift of $z=0.400$ while the SW cD has an spectroscopic redshift of $z=0.396$.

The relative difference in redshift can be translated in a relative velocity, $\delta v \approx 1200 \text{ km/s}$, a value that is consistent with the velocity in the simulation shown in figure 9. The same redshift difference can be observed when looking at the surrounding galaxies as can be seen from figure 10 suggesting that MACSJ0416 consists of two clusters moving against each other in a direction close to the line of sight and that are close enough so that the X-ray plasma is already undergoing dynamical friction.

8 A VERY FLAT CORE REGION

This cluster has an unusual flat profile at around 10-20 arcseconds. In Z13 it was already shown that the projected mass profile between 10 and 20 arcsec is extremely shallow. Our model confirms this result as shown in figure 6 with a break in the slope at a radius of ≈ 20 arcsec (about 80 kpc/h). The result is even more significant if the baryonic component is subtracted from the mass profile. In the very central region, and depending on the assumed model for the fiducial galaxies, the total reconstructed mass gradually increases again towards the centre. However, although the lensing data lacks the sensitivity to constrain the very central region ($r < 1$ kpc) we should expect an additional flattening of the profile in the very centre at least for the NE galaxy. This is suggested by the significant flattening that is also observed in the light profile of the NE cD galaxy as shown in figure 11 (meanwhile the SW cD galaxy does not show this feature, at least not in a pronounced way). The flattening in the galaxy is probably the result of scouring by a massive black hole (or black hole binary) at the centre of the galaxy (Postman et al. 2012b; Rusli et al. 2013; Thomas et al. 2014; Lopez-Cruz et al. 2014). Stars in radial trajectories that approach the centre of the galaxy would be ejected by the black hole(s) towards larger radii, flattening the brightness profile of the galaxy (Thomas et al. 2014). The impact parameter, r_b , defined as the radius at which the Sersic profile breaks, is about $r_b \approx 1$ kpc (see figure 11). According to Rusli et al. (2013), the radius r_b scales with the mass of the black hole. A similar correlation is observed between the black hole mass and the velocity dispersion of the galaxies Gebhardt et al. (2000). For the observed $r_b \approx 1$ kpc, the scaling laws in Rusli et al. (2013) predict a mass for the super massive black hole of $M_{BH} \approx 10^{10} M_{\odot}$. The existence of the black hole is supported as well by a very small enhancement of the X-ray signal at the centre of the NE cD galaxy.

The same black hole that scours the centre of the galaxy of stars would flatten as well the distribution of dark matter particles reducing the fraction of radial orbits towards the centre of the galaxy. Hence, we should expect also a flattening in the dark matter distribution in the very central region ($r < 1$ kpc). However, this mechanism could not explain the flattening at larger radii (15 – 100 kpc/h). More energetic phenomena, probably involving the past collision of the two clusters, are required in order to explain the plateau at $r \approx 10 - 20$ arcseconds (40-80 kpc/h). Other mechanisms play a role in determining the intrinsic shape of the profile in the central region. Adiabatic compression of the DM by the infalling baryons can enhance the density profile in the very central region Blumenthal et al. (1986); Gnedin et al. (2004). On the other hand, this effect is opposed by the same infalling baryons that can heat up the core by dynamical friction and can transfer the orbital energy of the infalling baryons to the DM El-Zant et al. (2004). AGN feedback can contribute also to the flattening of the central region Martizzi et al. (2012). However, all these effects act on scales up to 10-15 kpc and could not explain a flattening extending up to 100 kpc. The dynamics of the merger could have an impact on larger scales and offer an alternative explanation to the shape of the profile. However, a flattening of the scale observed in this cluster is difficult to explain

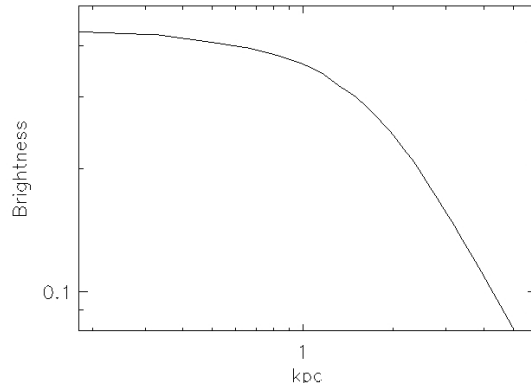


Figure 11. Brightness profile of the NE cD galaxy showing the break in the Sersic profile at around 1 kpc. The brightness is in arbitrary units.

with simulations. Ricker & Sarazin (2001) studies mergers of clusters for different mass ratios and impact parameters. Their simulations include both DM and baryons. For mass ratios similar to MACSJ0416, they find that the dark matter profiles are not strongly affected after the collision and the profiles don't show a plateau at any radius. The same result can be observed in our simulations as it is shown in figure 9 and also in simulations from our archive of merging clusters Molnar, Hearn & Stadel (2012), where both clumps conserve their cusps. In Dekel, Devor & Hetzroni (2003), the authors argue that merging of cuspy halos inevitably leads to a cusp, thus implying that the two subclusters in MACSJ0416 must have had their cusps suppressed before the merger by some mechanism. Simulations of collisions of cored clusters (with cores of about 100 kpc), suggest that the core can survive the collision Ritchie & Thomas (2002). However, these simulations do not explain how the core is formed. Despite the need of simulations to understand the role of merger dynamics on the profiles of cluster similar to MACSJ05416, simulations are often difficult to interpret, specially in the central region of clusters. Different codes may produce different results depending on their implicit assumptions. As shown in Mitchell et al. (2009), smoothed particle hydrodynamics (or SPH) N-body simulations tend to produce more massive cores than Eulerian mesh codes although the discrepancy gets reduced when the refinement level is increased in the mesh code.

Alternatively, if the DM is self-interacting, the probability of interaction increases with the speed of the DM particles. A cluster collision offers a unique opportunity to boost the chance of interaction from the increased relative velocity of the interacting particles. One interesting clue can be found in Rocha et al. (2013). In that work, the authors simulate large scale structure under the assumption that dark matter can self-interact (with a higher probability at the cores of haloes). Interestingly, for cross-sections $\sigma/m \approx 1 \text{ cm}^2/\text{g}$ they find that in halos of masses $M_{vir} = 2 \times 10^{14} M_{\odot}$ the profile exhibits a plateau corresponding to core scales of about 150 kpc. The plateau extends from the centre up to about 70 kpc and at the centre the density is about an order of magnitude lower than in the corresponding standard NFW profile. In our case, if the impact parameter of the two clusters is about 200 kpc, the chance of interaction between DM

particles should be smaller than in the case of a head-on collision. However, it is still important to emphasize how the characteristics of the cored profiles in Rocha et al. (2013) strikingly resemble the observed profiles in MACSJ0416 so this possibility still offers a possible interesting explanation. Moreover, the fact that this cluster went through a collision would imply that even a smaller than $1 \text{ cm}^2/\text{g}$ cross section could be enough to cause a similar effect since the increase in relative velocity due to the collision could compensate the decrease in the cross-section. A lower than $1 \text{ cm}^2/\text{g}$ value for σ/m is also preferred by observations of more relaxed clusters where such a flattening of the central region is not observed.

Finally, another probable mechanism that can contribute to disrupting the core are tidal forces. In figure 9, the DM haloes show an elongation. Since the initial model is symmetric the tidal effects must be present at the time we are witnessing this encounter. The effect that tidal forces have on stretching the cores of merging clusters will be studied in a subsequent paper.

It is not clear that the extent of these effects would still be sufficient to explain the observed profiles. More likely, a combination of different effects would be the most plausible explanation. If DM is self-interacting, a small cross section together with some of the mechanisms described above plus projection effects could lead to a flattening of the central region in colliding clusters. If DM self-interaction plays a significant role, similar shallow profiles should be observed in other post-collision clusters, in particular in the morphologically disturbed FF clusters, where the DM distribution can be inferred directly from gravitational lensing. Improved observations on this cluster will be available soon from a multiwavelengths perspective, in the optical with the remaining FF data (improved photo-z for the lensing systems and potentially new systems), in X-ray with already planned Chandra observations may reveal shocks, and a better location of the peaks in the X-ray emission; in radio with also planned deep VLA observations may reveal possible evidence of past merging activity and confirm the shock activity. Together they will throw some light on this interesting cluster.

9 CONCLUSIONS

We derive a free-form solution of MACSJ0416 that resembles those obtained with parametric methods. To first order, we find that the mass traces the light in this merging and elongated cluster. Some offsets between the DM and plasma are observed, in particular a very shallow soft dark matter halo surrounding each cD galaxy. The intrinsic shape of the soft haloes does not show the intrinsic symmetries assumed in parametric methods highlighting the need for free-form methods in these type of clusters. Our DM reconstructed distribution shows an elongation in the direction of a peak in the X-ray data suggesting that the lensing distortions may be sensitive also to the mass of the plasma. The two density profiles associated to each subhalo are almost identical suggesting a 1:1 ratio for this merging cluster. The profiles also exhibits a plateau at around 40-100 kpc which could be interpreted as the result of dynamical distortions of the subcluster cluster profiles, or projection effects but also as possible evidence of self interacting DM with an increased

probability of interaction during the collision. Detailed lensing observations of merging galaxy clusters, like those from the FF, together with more detailed simulations of merging clusters may help clarify this situation.

10 ACKNOWLEDGMENTS

J.M.D acknowledges support of the consolidator project CAD2010-00064 and AYA2012-39475-C02-01 funded by the Ministerio de Economía y Competitividad. JMD also acknowledges the hospitality of the Department of Physics and Astronomy at UPenn during part of this research. The scientific results reported in this article are based in part on data obtained from the Chandra Data Archive. We would like to thank Harald Ebeling for providing us with the code ASMOOTH (Ebeling, White & Rangarajan 2006) that was used to smooth the Chandra data.

This paper has been typeset from a $\text{T}_\text{E}\text{X}/\text{L}^\text{A}\text{T}_\text{E}\text{X}$ file prepared by the author.

REFERENCES

- Atek H. et al., 2014, *ApJ*, 786, 60
 Blumenthal G. R., Faber S. M., Flores R., Primack J. R., 1986, *ApJ*, 301, 27
 Broadhurst, et al., 2005a, *ApJ*, 621, 53
 Coe D. et al., 2013, *ApJ*, 762, 32
 de Laix A. A., Scherrer R. J., Schaefer R. K., 1995, *ApJ*, 452, 495
 Dekel A., Devor J., Hetzroni G., 2003, *MNRAS*, 341, 326
 Diego J. M. et al., 2014, *ArXiv e-prints*
 Diego J. M., Protopapas P., Sandvik H. B., Tegmark M., 2005a, *MNRAS*, 360, 477
 Diego J. M., Sandvik H. B., Protopapas P., Tegmark M., Benítez N., Broadhurst T., 2005b, *MNRAS*, 362, 1247
 Diego J. M., Tegmark M., Protopapas P., Sandvik H. B., 2007, *MNRAS*, 375, 958
 Ebeling H., Ma C.-J., Barrett E., 2014, *ApJS*, 211, 21
 Ebeling H., White D. A., Rangarajan F. V. N., 2006, *MNRAS*, 368, 65
 El-Zant A. A., Hoffman Y., Primack J., Combes F., Shlosman I., 2004, *ApJ*, 607, L75
 Gebhardt K. et al., 2000, *ApJ*, 539, L13
 Gnedin O. Y., Kravtsov A. V., Klypin A. A., Nagai D., 2004, *ApJ*, 616, 16
 Halkola A., Seitz S., Pannella M., 2006, *MNRAS*, 372, 1425
 Hlavacek-Larrondo J. et al., 2013, *ApJ*, 777, 163
 Jauzac M. et al., 2014, *ArXiv e-prints*
 Johnson T. L., Sharon K., Bayliss M. B., Gladders M. D., Coe D., Ebeling H., 2014, *ArXiv e-prints*
 Kahlhoefer F., Schmidt-Hoberg K., Frandsen M. T., Sarkar S., 2014, *MNRAS*, 437, 2865
 Kneib J.-P., Ellis R. S., Smail I., Couch W. J., Sharples R. M., 1996, *ApJ*, 471, 643
 Limousin M. et al., 2007, *ApJ*, 668, 643
 Lopez-Cruz O., Anorve C., Birkinshaw M., Worrall D. M., Ibarra-Medel H. J., Torres-Papaqui J. P., Barkhouse W. A., Motta V., 2014, *ArXiv e-prints*
 Mann A. W., Ebeling H., 2012, *MNRAS*, 420, 2120

- Markevitch M., Gonzalez A. H., Clowe D., Vikhlinin A., Forman W., Jones C., Murray S., Tucker W., 2004, *ApJ*, 606, 819
- Martizzi D., Teyssier R., Moore B., Wentz T., 2012, *MNRAS*, 422, 3081
- Mastropietro C., Burkert A., 2008, *MNRAS*, 389, 967
- Merten J. et al., 2014, *ArXiv e-prints*
- Mitchell N. L., McCarthy I. G., Bower R. G., Theuns T., Crain R. A., 2009, *MNRAS*, 395, 180
- Molnar S. M., Broadhurst T., 2014, *ArXiv e-prints*
- Molnar S. M., Hearn N. C., Stadel J. G., 2012, *ApJ*, 748, 45
- Nakajima T., Morikawa M., 2007, *ApJ*, 655, 135
- Navarro J. F., Frenk C. S., White S. D. M., 1997, *ApJ*, 490, 493
- Nieuwenhuizen T. M., Morandi A., 2013, *MNRAS*, 434, 2679
- Ponente P. P., Diego J. M., 2011, *A&A*, 535, A119
- Postman M. et al., 2012a, *ApJS*, 199, 25
- Postman M. et al., 2012b, *ApJ*, 756, 159
- Richard J. et al., 2014, *ArXiv e-prints*
- Ricker P. M., Sarazin C. L., 2001, *ApJ*, 561, 621
- Ritchie B. W., Thomas P. A., 2002, *MNRAS*, 329, 675
- Rocha M., Peter A. H. G., Bullock J. S., Kaplinghat M., Garrison-Kimmel S., Oñorbe J., Moustakas L. A., 2013, *MNRAS*, 430, 81
- Rusli S. P., Erwin P., Saglia R. P., Thomas J., Fabricius M., Bender R., Nowak N., 2013, *AJ*, 146, 160
- Sendra I., Diego J. M., Broadhurst T., Lazkoz R., 2014, *MNRAS*, 437, 2642
- Sharon K., Broadhurst T. J., Benitez N., Coe D., Ford H., ACS Science Team, 2005, in *IAU Symposium*, Vol. 225, *Gravitational Lensing Impact on Cosmology*, Mellier Y., Meylan G., eds., pp. 167–172
- Spergel D. N., Steinhardt P. J., 2000, *Physical Review Letters*, 84, 3760
- Springel V., Farrar G. R., 2007, *MNRAS*, 380, 911
- Thomas J., Saglia R. P., Bender R., Erwin P., Fabricius M., 2014, *ApJ*, 782, 39
- Zheng W. et al., 2014, *ArXiv e-prints*
- Zitrin A. et al., 2011, *ApJ*, 742, 117
- Zitrin A. et al., 2013, *ApJ*, 762, L30
- Zitrin A. et al., 2012, *ApJ*, 749, 97

APPENDIX A: COMPILATION OF ARC STAMPS AND POSITIONS

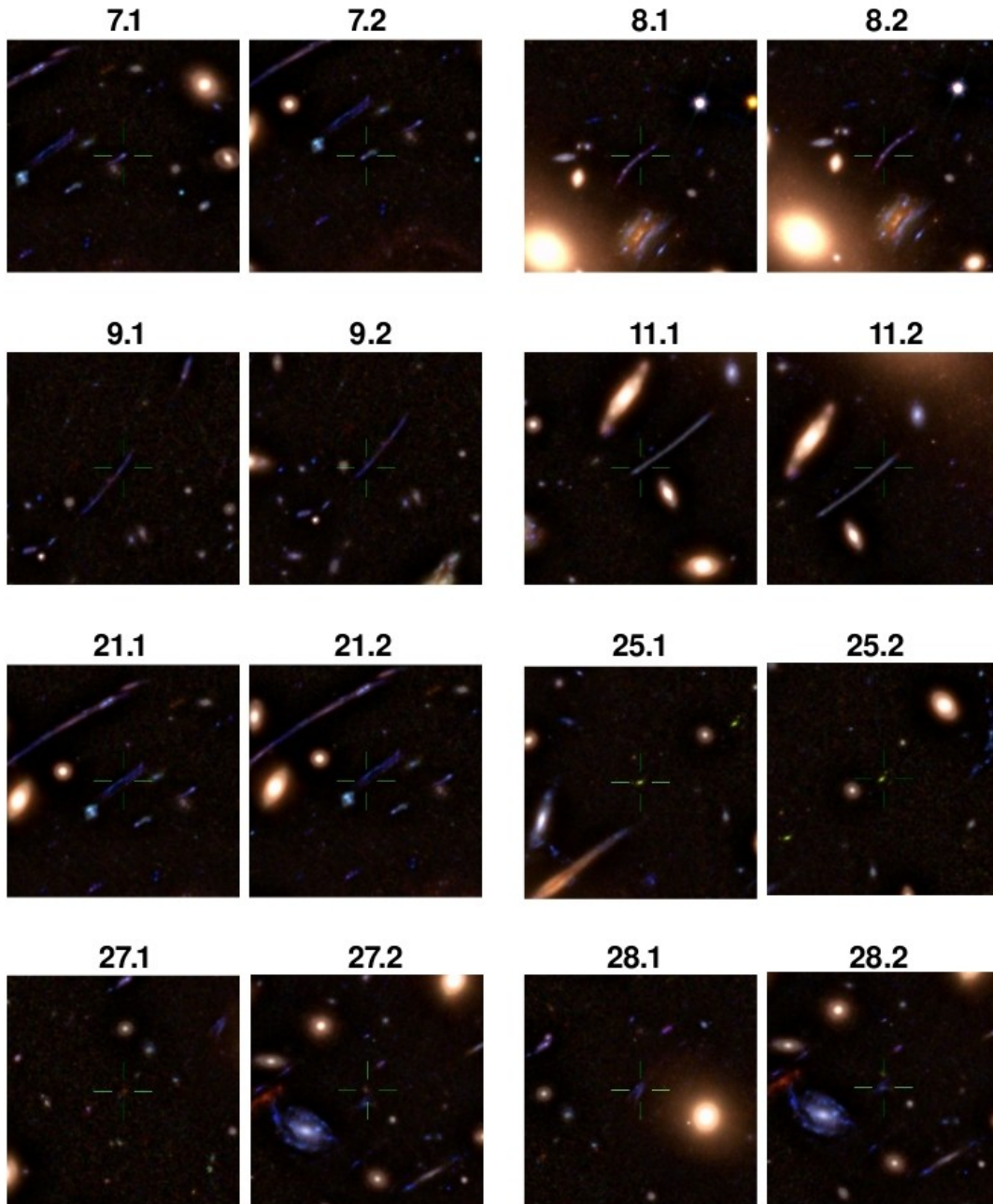


Figure A1. Images have been filtered to reduce light glare from member galaxies.

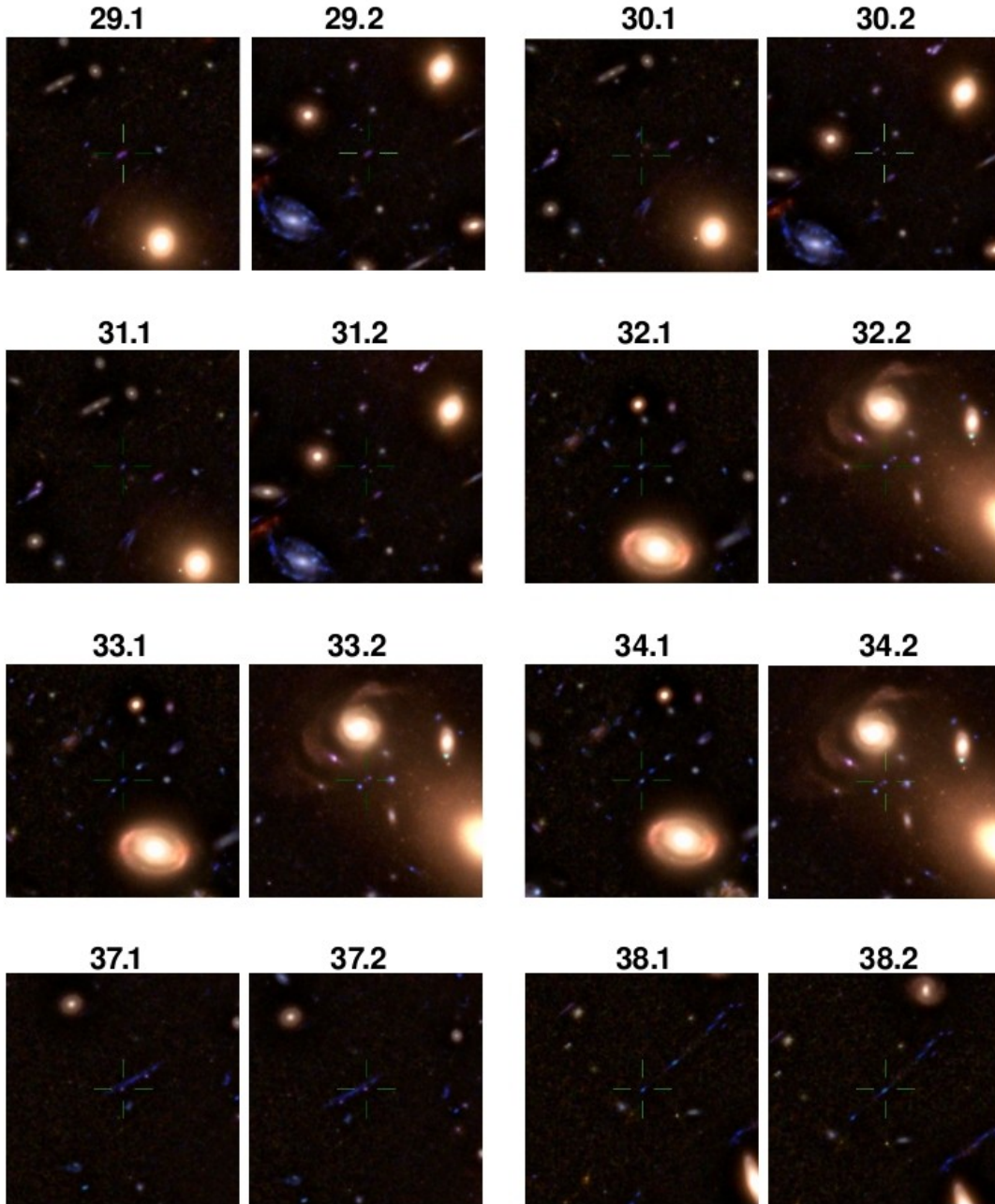


Figure A2. Light from member galaxies has been reduced through a high-pass filter.

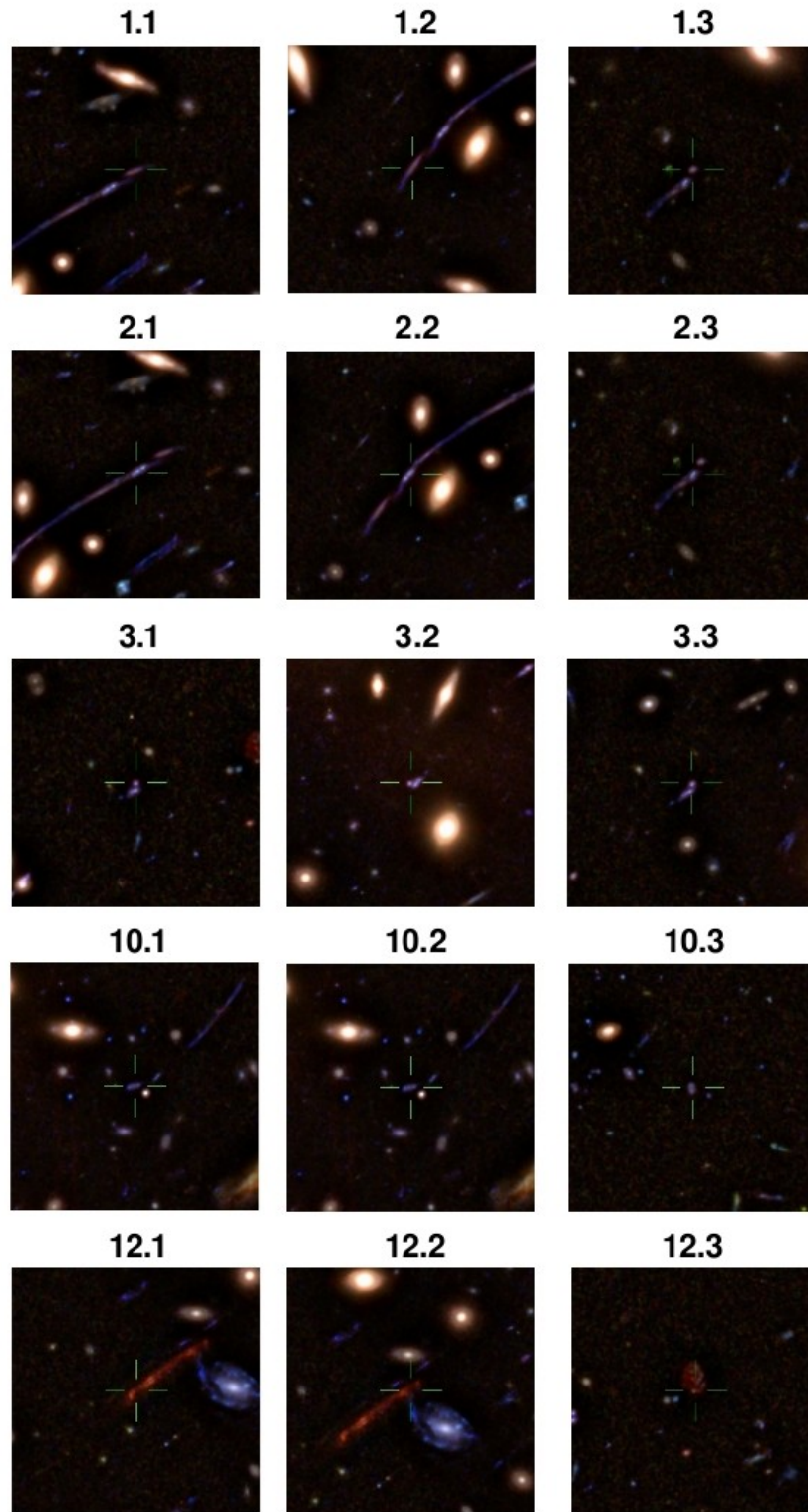


Figure A3. Light from member galaxies has been reduced through a high-pass filter.

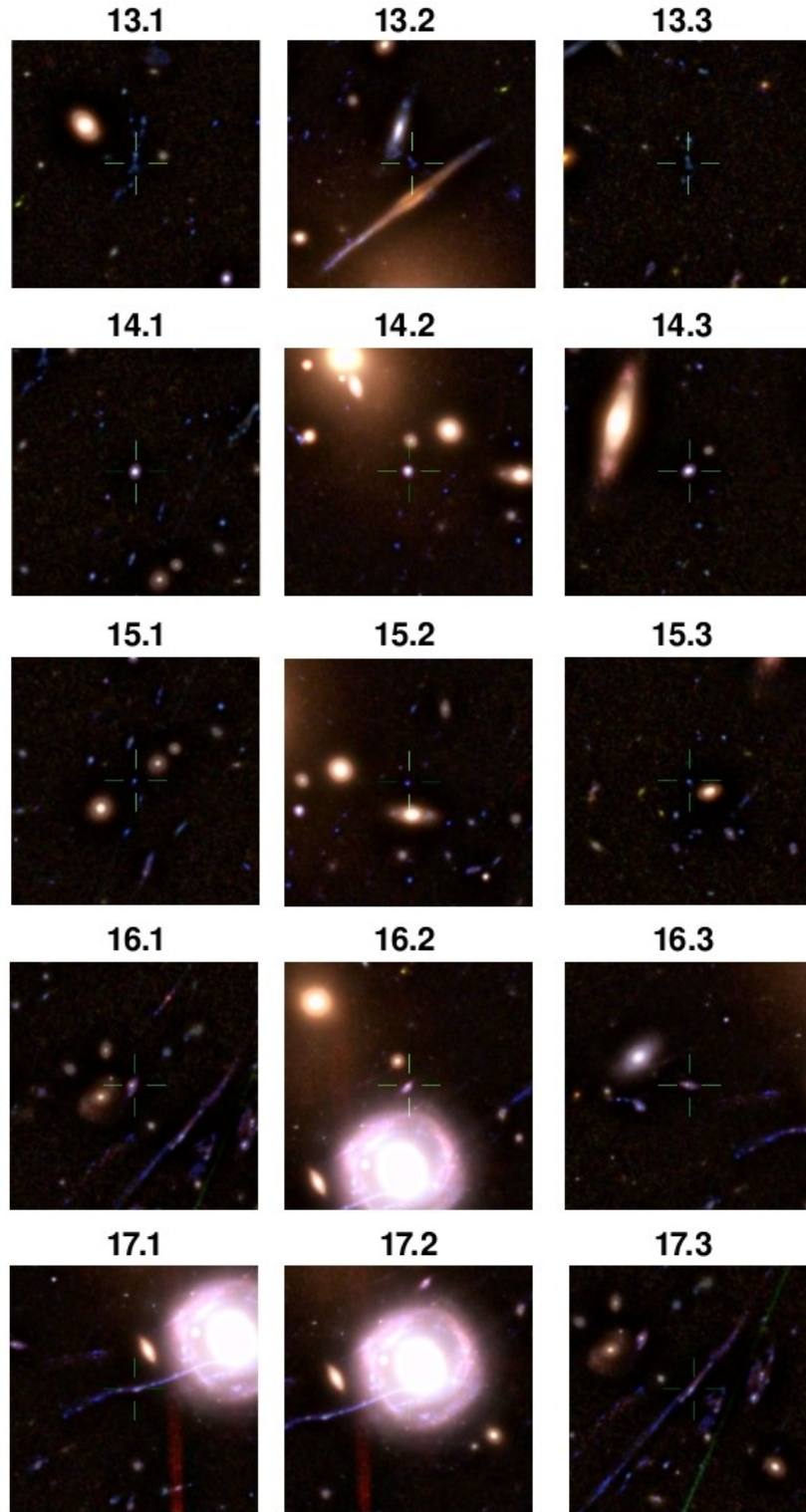


Figure A4. Light from member galaxies has been reduced through a high-pass filter.

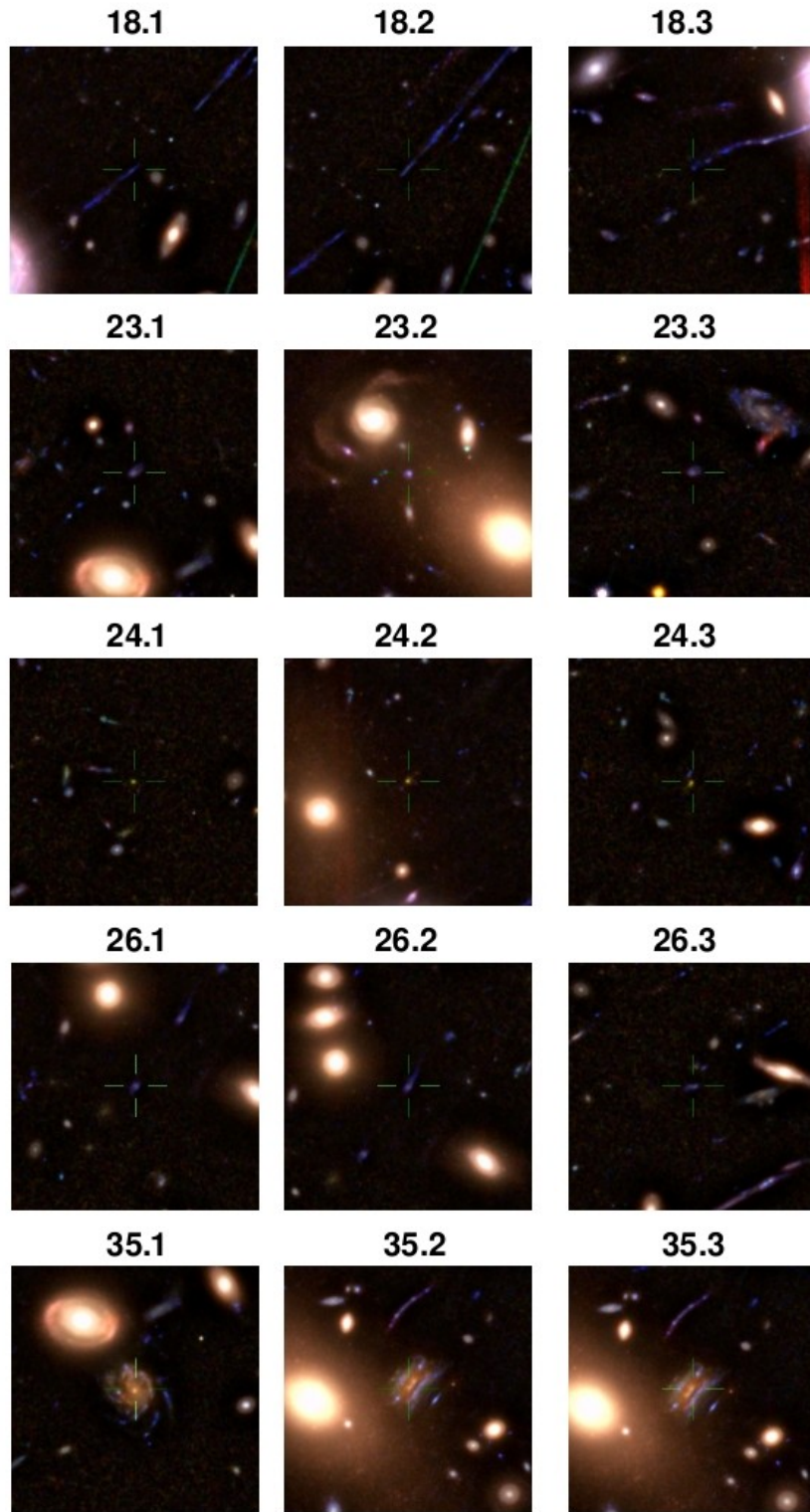


Figure A5. Light from member galaxies has been reduced through a high-pass filter.

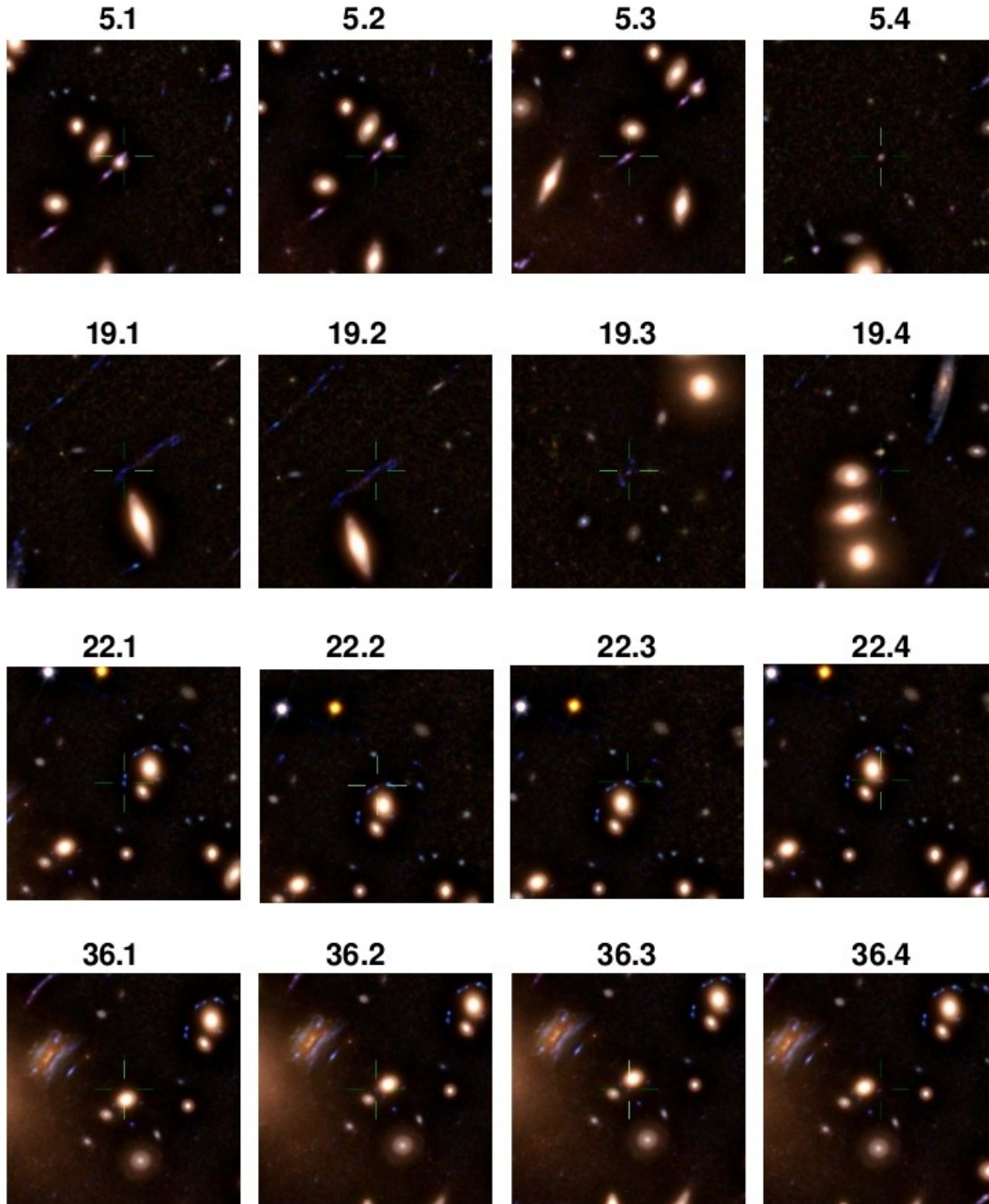


Figure A6. Light from member galaxies has been reduced through a high-pass filter.

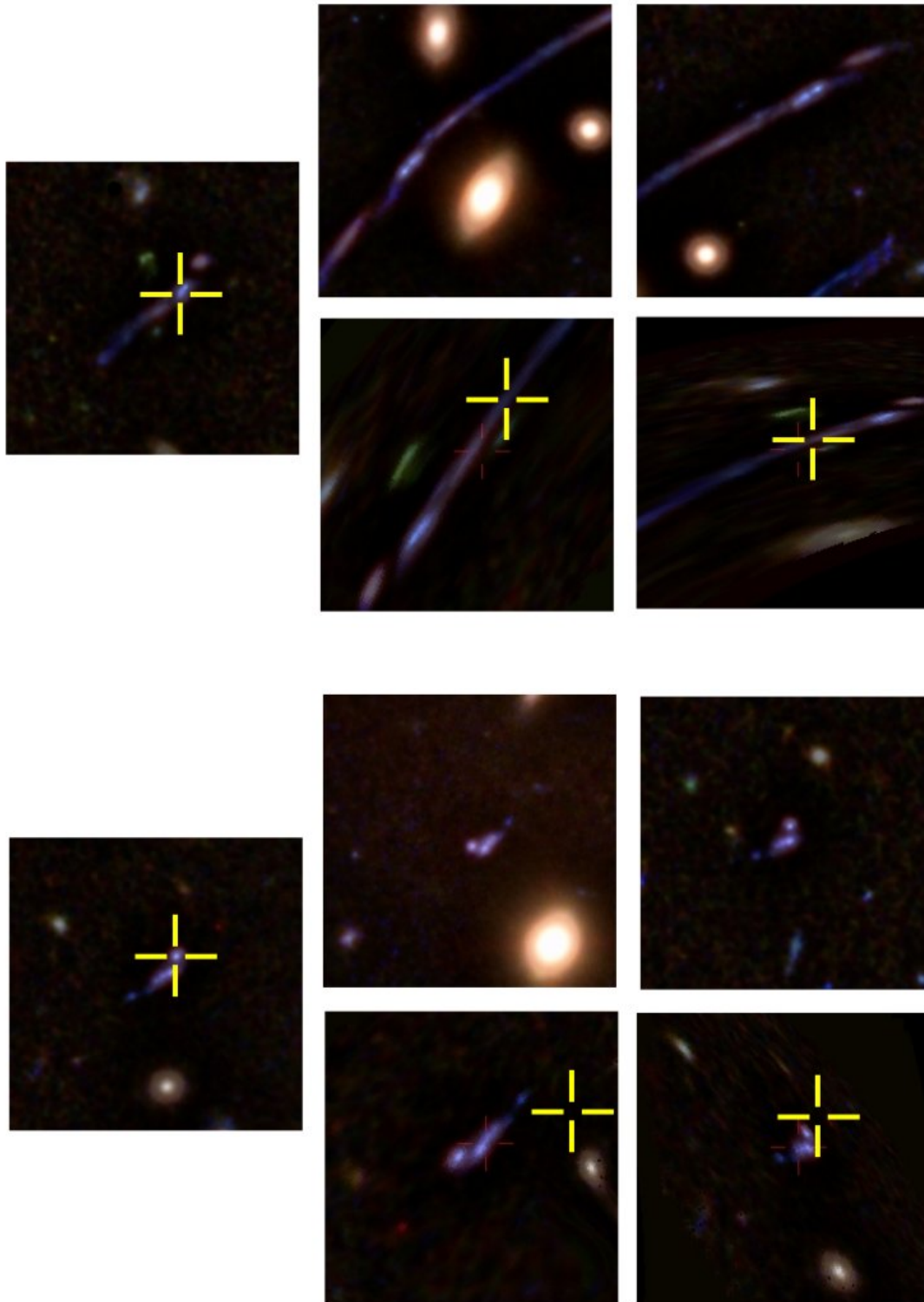


Figure A7. Top group, released system 1 (and 2). The image on the left is the one used to delense the galaxy into the source plane. On the right we show the observed (top) and predicted (bottom) counterimages. Bottom group, like the top group but for the released system 3 (and 4). The crosses mark the observed positions. We use the model in case ii) for the predicted images. In all cases the field of view is 7.2 arcseconds.

Table A1. Full strong lensing data set. The first column shows system ID following the original notation of Z13. The second and third columns show the coordinates of each arclet. Column 4 includes the redshifts used in our study (taken from Z13 when appropriate). Some of these redshifts are photometric and some are based on color and/or predicted by the lens model. The last column contains additional useful information. In this column, gz indicates that the redshift has been derived by the lens model. System 4 and system 3 are almost overlapping in position and could be in fact the same system but are treated as two different systems following Z13. Candidates marked with (*) correspond to new arclet candidates identified in this work. Arclet 12.3 is found at the position predicted by Z13. Due to the possibility of confusion by multiple faint arclets with similar colors and falling into the same region, we have not used the following arclets from Z13 7.3, 9.3 10.3,11.3, 12.3(updated), 15.3(updated), 21.3. Systems 6 and 20 from Z13 have been discarded completely due to bad color agreement after adding the new IR data.

ID	RAJ2000(h:m:s)	DECJ2000(d:m:s)	z	Notes
1.1	04:16:09.780	-24:03:41.73	1.896	spect z
1.2	04:16:10.435	-24:03:48.75	1.896	
1.3	04:16:11.365	-24:04:07.21	1.896	
2.1	04:16:09.884	-24:03:42.77	1.8	
2.2	04:16:10.321	-24:03:46.93	1.8	
2.3	04:16:11.394	-24:04:07.86	1.8	
3.1	04:16:07.388	-24:04:01.62	2.25	
3.2	04:16:08.461	-24:04:15.53	2.25	
3.3	04:16:10.036	-24:04:32.56	2.25	
4.1	04:16:07.398	-24:04:02.01	2.25	Same as 3.1?
4.2	04:16:08.437	-24:04:15.53	2.25	Same as 3.2?
4.3	04:16:10.051	-24:04:33.08	2.25	Same as 3.3?
5.1	04:16:07.773	-24:04:06.24	2.3	
5.2	04:16:07.839	-24:04:07.21	2.3	
5.3	04:16:08.043	-24:04:10.01	2.3	
5.4	04:16:10.454	-24:04:37.05	2.3	
7.1	04:16:09.552	-24:03:47.13	2.0	
7.2	04:16:09.752	-24:03:48.82	2.0	
8.1	04:16:08.783	-24:03:58.05	2.4	
8.2	04:16:08.840	-24:03:58.83	2.4	
9.1	04:16:06.486	-24:04:42.90	2.3	
9.2	04:16:06.605	-24:04:44.78	2.3	
10.1	04:16:06.244	-24:04:37.76	2.3	
10.2	04:16:06.833	-24:04:47.12	2.3	
10.3	04:16:08.807	-24:05:01.94	2.3	
11.1	04:16:09.410	-24:04:13.32	0.8	
11.2	04:16:09.196	-24:04:11.11	0.8	
12.1	04:16:09.230	-24:04:25.74	2.5	
12.2	04:16:09.011	-24:04:23.72	2.5	
12.3	04:16:06.956	-24:04:00.57	2.5	New(p12.3)
13.1	04:16:06.619	-24:04:22.03	3.0	
13.2	04:16:07.711	-24:04:30.61	3.0	
13.3	04:16:09.681	-24:04:53.56	3.0	
14.1	04:16:06.296	-24:04:27.62	1.7	
14.2	04:16:07.450	-24:04:44.26	1.7	
14.3	04:16:08.598	-24:04:52.78	1.7	
15.1	04:16:06.292	-24:04:33.67	2.0	
15.2	04:16:07.065	-24:04:42.90	2.0	
15.3	04:16:09.175	-24:04:58.71	2.0	New(*)
16.1	04:16:05.774	-24:04:51.22	2.0	
16.2	04:16:06.799	-24:05:04.35	2.0	
16.3	04:16:07.583	-24:05:08.77	2.0	
17.1	04:16:07.170	-24:05:10.91	2.5	
17.2	04:16:06.866	-24:05:09.55	2.5	
17.3	04:16:05.599	-24:04:53.69	2.5	
18.1	04:16:06.258	-24:05:03.24	2.8	
18.2	04:16:06.016	-24:05:00.06	2.8	
18.3	04:16:07.416	-24:05:12.28	2.8	
19.1	04:16:10.909	-24:03:41.08	2.7	
19.2	04:16:10.777	-24:03:39.85	2.7	
19.3	04:16:11.925	-24:04:00.91	2.7	
19.4	04:16:11.580	-24:03:52.23	2.7	New(*)

Table A1. cont.

ID	RAJ2000(h:m:s)	DECJ2000(d:m:s)	z	Notes
21.1	04:16:09.813	-24:03:46.67	2.6	
21.2	04:16:09.865	-24:03:47.32	2.6	
22.1	04:16:08.278	-24:04:01.07	1.8	
22.2	04:16:08.204	-24:03:59.28	1.8	
22.3	04:16:08.162	-24:03:59.22	1.8	
22.4	04:16:08.152	-24:04:00.87	1.8	New(*)
23.1	04:16:10.691	-24:04:19.56	2.0	
23.2	04:16:09.505	-24:03:59.87	2.0	
23.3	04:16:08.242	-24:03:49.47	2.0	
24.1	04:16:08.413	-24:05:07.85	5.0	New
24.2	04:16:06.820	-24:04:58.83	5.0	New
24.3	04:16:05.517	-24:04:38.16	5.0	New
25.1	04:16:07.385	-24:04:27.03	4.0	New
25.2	04:16:07.028	-24:04:24.00	4.0	New
26.1	04:16:11.551	-24:04:01.05	2.0	New
26.2	04:16:11.394	-24:03:57.75	2.0	New
26.3	04:16:10.136	-24:03:37.95	2.0	New
27.1	04:16:10.056	-24:04:38.79	4.0	New
27.2	04:16:08.658	-24:04:23.49	4.0	New
28.1	04:16:09.683	-24:04:35.37	2.0	New
28.2	04:16:08.662	-24:04:24.15	2.0	New
29.1	04:16:09.578	-24:04:32.19	2.0	New
29.2	04:16:08.605	-24:04:22.11	2.0	New
30.1	04:16:09.705	-24:04:32.79	2.0	New
30.2	04:16:08.632	-24:04:20.88	2.0	New
31.1	04:16:09.718	-24:04:31.71	2.0	New
31.2	04:16:08.651	-24:04:20.64	2.0	New
32.1	04:16:10.824	-24:04:20.43	2.0	New
32.2	04:16:09.620	-24:04:00.27	2.0	New
33.1	04:16:10.886	-24:04:21.15	2.0	New
33.2	04:16:09.598	-24:03:59.97	2.0	New
34.1	04:16:10.921	-24:04:21.63	2.0	New
34.2	04:16:09.582	-24:03:59.82	2.0	New
35.1	04:16:10.575	-24:04:28.02	1.65	New gz
35.2	04:16:08.803	-24:04:02.43	1.65	New gz
35.3	04:16:08.780	-24:04:02.06	1.65	New gz
36.1	04:16:08.509	-24:04:03.86	2.0	New
36.2	04:16:08.547	-24:04:04.64	2.0	New
36.3	04:16:08.514	-24:04:04.95	2.0	New
36.4	04:16:08.441	-24:04:04.49	2.0	New
37.1	04:16:07.931	-24:04:54.42	2.0	New
37.2	04:16:07.841	-24:04:53.73	2.0	New
38.1	04:16:11.271	-24:03:38.85	2.0	New
38.2	04:16:11.148	-24:03:37.41	2.0	New

Table A2. Arclets from Z13 that are not used in this work. Systems 6 and 20 where removed completely.

ID	RAJ2000(h:m:s)	DECJ2000(d:m:s)	Notes
7.3	04:16:11.308	-24:04:15.99	Many candidates nearby
9.3	04:16:09.149	-24:05:01.23	Many candidates nearby. Far from prediction
10.3	04:16:09.818	-24:04:58.69	The alternative 10.3 works better
11.3	04:16:08.214	-24:03:57.66	No predicted 3rd counterimage
12.3	04:16:06.989	-24:04:03.57	Red galaxy nearby fits position better (and color)
15.3	04:16:08.560	-24:04:55.38	Far from model prediction
21.3	04:16:11.047	-24:04:07.73	Far from model prediction